C Journal of Carbon Research

MDPI

Article

Synthesis of Ni@SiC/CNFs Composite and Its Microwave-Induced Catalytic Activity

Haibo Ouyang *, Jiaqi Liu, Cuiyan Li, Leer Bao, Tianzhan Shen and Yanlei Li

Key Laboratory for Green Manufacturing & Functional Application of Inorganic Materials, School of Materials Science and Engineering, Shaanxi University of Science and Technology, Xi'an 710021, China; JiaqiLiu068@163.com (J.L.); licuiyan@sust.edu.cn (C.L.); theory2w@163.com (L.B.); tzshen2243@163.com (T.S.); 15829291050@163.com (Y.L.)

* Correspondence: ouyanghb@sust.edu.cn

Abstract: Carbon nanomaterials are promising microwave catalytic materials due to their abundant inhomogeneous interfaces capable of producing ideal interfacial polarization and multiple relaxation, which are favorable for microwave attenuation and dissipation. However, the microwave absorption performance of carbon materials is not ideal in practical applications due to poor impedance matching and single dielectric loss. To solve this problem, a ternary system of "carbon-magnetic" Ni@SiC/CNFs (C/Ni, C/SiC) composites was synthesized by electrostatic spinning, and they efficiently degraded methylene blue under microwave radiation. The results imply that the catalyst Ni@SiC/CNFs with a double-shell structure gave a 99.99% removal rate in 90 s for the degradation of methylene blue under microwave irradiation, outperforming the C/Ni and C/SiC and most other reported catalysts in similar studies. On the one hand, the possible mechanism of the methylene blue degradation should be ascribed to the fact that the double-shell structure increases the polarization source of the material, resulting in excellent microwave absorption properties; and on the other, the in situ generation of ·OH and O_2^- active species under microwave radiation and the synergistic coupling effect of metal plasma greatly improved the degradation efficiency of methylene blue. The findings of this study could provide a valuable reference for the green degradation of industrial dye wastewater and its sustainable development process.

Keywords: double-shell catalyst; electrospinning; microwave irradiation; degradation; active species; plasma

Citation: Ouyang, H.; Liu, J.; Li, C.; Bao, L.; Shen, T.; Li, Y. Synthesis of Ni@SiC/CNFs Composite and Its Microwave-Induced Catalytic Activity. *C* **2024**, *10*, 72. https://doi.org/10.3390/c10030072

Academic Editor: Athanasia Tolkou

Received: 30 June 2024
Revised: 6 August 2024
Accepted: 7 August 2024
Published: 9 August 2024

1. Introduction

With the rapid development of the economy and the increasing growth in population, the quantity of wastewater produced and its overall pollution load is continuously increasing worldwide [1–3]. According to reports from the United Nations World Water Development, over 80 percent of wastewater worldwide is released into the environment without treatment. Untreated wastewater not only jeopardizes human health but also seriously pollutes the ecological environment and adversely affects various economic activities [4,5]. Organic dyes are widely used in various industries (e.g., textile, pharmaceutical, food, cosmetic, plastic, photographic, and paper industries) and are an important source of water pollution; how to reduce the water pollution caused by organic dyes has attracted widespread attention from many different sectors [6–8].

Currently, adsorption, coagulation, advanced oxidation, and membrane separation are widely used for the removal of dyes from wastewater [9,10]. In recent years, advanced oxidation processes (AOPs) have made remarkable progress in the field of wastewater treatment [11]. The degradation of dyes by AOPs contributes to the in situ generation of free radicals with high oxidizing activity (·OH, O_2^-, SO_4^-) [12]. These radicals react non-selectively with most organic matter, resulting in the extensive degradation or mineralization of pollutants [13–15].

Microwave-enhanced AOPs can greatly improve the degradation rate and shorten the reaction time, since they have the ability to induce a hot spot effect, plasma discharge effect, and photoelectric effect in the microwave field. (i) The hot spots are a microplasma region on the catalyst surface where temperatures can reach over 1200 °C, promoting faster production of active species and oxidation of organic matter [16]. Qi et al., Hu et al., Garcia-Costa et al., Lei et al., and Shen et al. utilized the microwave hot spot effect to efficiently degrade different organic pollutants [17–21]. (ii) When microwaves act on certain tips or metals with special shapes or sizes, a charge builds up at the tip, causing the nearby electric field to be stronger than the air field, and thus a plasma discharge phenomenon occurs [22]. Qian et al., Zhao et al., Xu et al., and Zhang et al. used the plasma discharge effect generated under a microwave for the efficient treatment of refractory organic matter as well as white pollution [22–25]. (iii) Catalysts with semiconducting properties (e.g., transition metal oxides, semiconductors, and ferromagnetic metals) generate hole–electron pairs upon MW excitation, and the excited h^+ and e^- can migrate to the catalyst surface to participate in redox reactions [17,26,27]. Nowadays, the catalytic activity of many materials can be induced by microwave irradiation. When the MW irradiates these materials, the interaction between them can rapidly generate heat to produce a large number of active sites for the enhanced absorption and conversion of MW energy. Thus, it is a critical issue to develop microwave-active catalysts with strong microwave absorption ability and efficient microwave energy transfer ability [28–30].

Carbon nanomaterials are rich in hole structure, which can increase the electron transport path and improve the conductive loss. Meanwhile, the non-uniform structure of the phase interface can generate abundant interfacial polarization and multiple relaxation to enhance microwave attenuation [31,32]. However, due to poor impedance matching and single dielectric loss, the microwave absorption performance of carbon materials is not very ideal [33]. "Carbon-magnetic" composites are a good way to solve this problem. By introducing magnetic metals and microwave absorbers with high dielectric loss into carbon matrix materials, which can be enriched with a single microwave loss mechanism while obtaining ideal magnetic loss, impedance matching can be improved and microwave attenuation capability can be enhanced [34]. Magnetic materials (such as Fe, Co, Ni, and corresponding alloys) are ideal complementary materials because of their higher permeability, saturation magnetization, and snoek limit [35–37]. When the microwave irradiates the metal, a unique discharge phenomenon occurs, which can realize the coupling of the thermal effect and the plasma effect. Li [33] et al. synthesized the rod-like Ni@C composite, which has good microwave absorption and high reuse efficiency. SiC is an ideal microwave absorber because of its high microwave absorption characteristics in the gigahertz frequency. The superior thermal conductivity means it can still be used as a catalyst carrier at high temperatures. However, due to its inherent low conductivity and single polarization characteristics, SiC needs to be combined with different magnetic materials or carbon-based materials to enhance electrical conductivity and enrich its polarization types to improve its microwave absorption performance [38]. Samarjit Singh et al. prepared a Ni/SiC/graphene composite material with a minimum reflection loss of −59.15 dB, showing good microwave absorption performance [39].

Based on the above ideas, we propose a novel Ni@SiC/CNFs catalyst for MW-AOP. Carbon fibers, as supporting materials, in addition to excellent microwave absorption properties, also have a high electron mobility, which can promote charge separation/electron transfer and improve catalytic oxidation performance. SiC and Ni nanoparticles generate hole–electron pairs and strong plasma discharge under microwave irradiation. At the same time, the reaction of hole–electron pairs with O_2 and H_2O in the air generates strong oxidizing groups, which enhances the chemical reaction in degradation and improves the degradation efficiency. The hot spots and plasma generated by this discharge phenomenon can increase the degradation rate by reducing the presence of contaminants on the material and decreasing their participation in the chemical reaction time.

In this work, the Ni@SiC/CNF composites as MV-AOP catalysts were synthesized by the electrostatic spinning method. The morphology, microstructure, and phase composition of the Ni@SiC/CNFs were characterized through complementary analytical ways. The microwave catalytic performance of the Ni@SiC/CNFs was evaluated with MB as the target containment. The catalytic mechanism was proposed to explain the synergistic effect of the Ni@SiC/CNF catalyst under microwave irradiation.

2. Materials and Methods

2.1. Synthesis of Ni@SiC/CNFs

The Ni@SiC/CNF composites were prepared by electrostatic spinning combined with high-temperature carbonization (CNFs are carbon nanofibers, and SiC is silicon carbide). First of all, the precursor solution containing 10 mL of N, N-Dimethylformamide (DMF), 1.0 g of polyvinylpyrrolidone (PAN), 0.16 g of polycarbosilane (PCS), 1.7 mol of ($Ni(CH_3COO)_2$), and 2 mol of thiourea was configured. Subsequently, the prepared precursor solution was loaded into a 10 mL plastic syringe and injected at a flow rate of 7 μL/min, setting a distance of 17 cm between the needle and the receiver, a voltage of 17 kV, and a rotational speed of 600 r/min, to ultimately obtain a primed polymer fiber membrane. To maintain fiber morphology, the as-spun polymer nanofibers were subsequently pre-sintered at 280 °C for 2 h in the air followed by further carbonization at 1400 °C for 1 h under Ar atmosphere. Finally, the Ni@SiC/CNF (NSC) composites were obtained. By changing the content of PCS(0 g) in the precursor solution, the C/Ni (NC) composite material was prepared. By changing the content of ($Ni(CH_3COO)_2$) (0 mol) and thiourea (0 mol) in the precursor solution, the C/SiC (SC) composite material was prepared. Figure 1 is the schematic diagram of the preparation of the different composite materials.

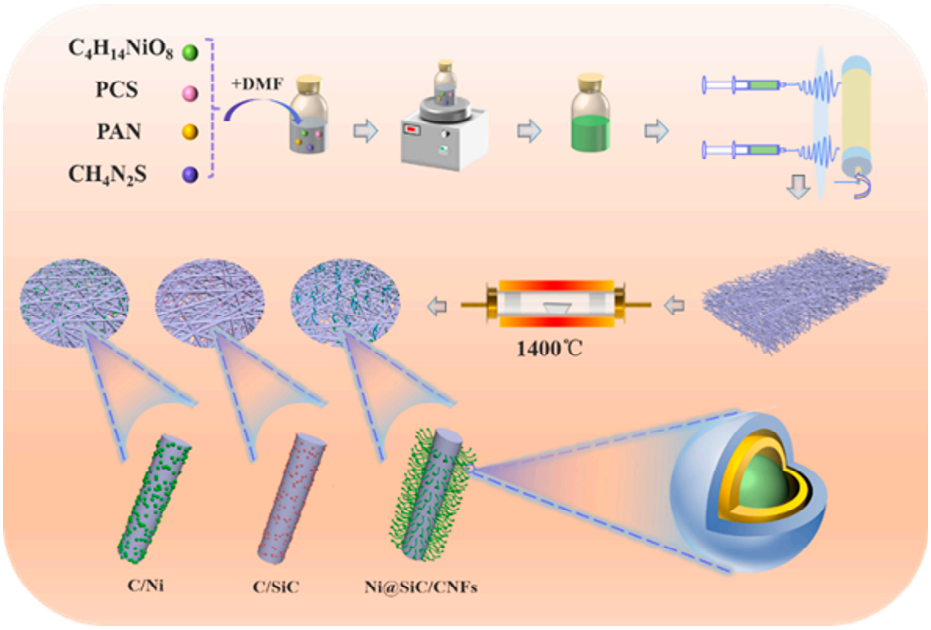

Figure 1. The flow diagram of preparing Ni@SiC/CNF, C/Ni, and C/SiC composites.

2.2. Characterization

The crystal structure of the sample was investigated using a powder X-ray diffractometer (XRD, Rigaku D/max-2200PC) with Cu Kα (λ = 0.15418 nm) radiation.

The morphology of the samples was observed using a field-emission scanning electron microscope (Chiyoda City, Japan, Hitachi, FE-SEM, S-4800).

XPS can be used for qualitative and quantitative analysis of the elements contained in the sample, and can also characterize the surface composition and chemical state of the sample.

High-resolution transmission electron microscopy (HRTEM) combined with energy dispersive spectroscopy (EDS) observation was performed on a Thermos Fisher Scientific, USA FEI Tecnai G2 F20S-TWIN system at 200 kV.

The molecular structure of the prepared samples was analyzed using a Renishaw-invia Raman instrument manufactured by Renishaw (London, UK), with lasers: 532 nm; 785 nm, wavelength range: 100–4000 cm^{-1}, optical plate size: 1–2 μm, and power: 0.005%–100% adjustable.

The UV–vis absorption spectra of the degradation were recorded on a UV/vis/NI R Spectrophotometer (LAMBDA950, PerkinElmer, Shanghai, China).

The dielectric property and magnetic permeability of the catalysts were analyzed by a vector network analyzer (Agilent 85071 E, Santa Clara, CA, USA). The block samples made in this study were tested by the waveguide method. The test range is X-band (2–18 GHz), and the samples are cut into cubic samples of 22.86 mm in length, 10.16 mm in width, and 1–3 mm in height.

2.3. Degradation Experiment Using Microwave

To examine the catalytic activity of the catalysts, degradation experiments were carried out using a controllable MW oven (WD750B, Galanz Company, Foshan, China) equipped with a self-made glass reactor and a condensing tube. The procedure was as follows: a methylene blue solution was prepared at a concentration of 20 mg/L; 20 mL of methylene blue solution and 20 mg of catalyst were added to a 50 mL reaction vessel, and degradation experiments were carried out.

The Teflon reaction vessel was followed by microwave irradiation (450 W, 2450 MHz). Upon the desired reaction time, the mixture was cooled to room temperature. The reaction mixture was then analyzed to evaluate the degradation efficiency by an ultraviolet spectrophotometer (UV–vis, UV-2450, SHIMADZU, Kyoto City, Japan). The removal rate of MB was calculated using the following formula:

$$Removal\ rate\ (\%) = \frac{C_0 - C_t}{C_0} \times 100\%$$

C_0 and C_t are the initial concentration and the concentration after treatment time t of MB solution, respectively. Figure S1 is a schematic diagram of a microwave-assisted catalytic reactor.

3. Results

3.1. Microstructure and Morphology

As depicted in Figure 2a, the NSC catalyst shows three clear and sharp diffraction peaks at 2θ = 26°, 35.6°, and 45.5°, corresponding to the (002) crystal plane of C, (111) crystal plane of SiC, and (121) crystal plane of Ni, respectively. The corresponding crystal sizes are 23.2 nm, 29.6 nm, and 27.7 nm. The NC and SC catalysts only have the carbon diffraction peak and the corresponding Ni diffraction peak and SiC diffraction peak. The diffraction peak intensity of SiC is lower for the SC catalysts compared to the NSC catalysts. This is because the intervention of Ni can provide a more catalytic effect for the generation of SiC. At high temperatures, C and Si in the composites are solidly dissolved in the molten Ni particles, and under the catalysis of Ni, the reaction between C and Si occurs to generate SiC. Therefore, the introduction of Ni in the NSC catalysts can provide a more catalytic effect for the generation of SiC, and generate more SiC. In addition, the SC catalyst corresponds to the Mantou peak of carbon at 26°, while NC and NSC both show a sharp diffraction peak of C, indicating that Ni particles play a major role in the catalytic graphitization of composites at high temperatures. To prove the above conjecture, the graphitization of carbon was further confirmed using Raman spectroscopy (Figure 2b). Two typical carbon peaks at 1345 cm^{-1} and 1592 cm^{-1} were observed, corresponding to the D band and G band of carbon [40]. It can be found that the R-value (ID/IG) of SC was the highest at 0.924, while that of NSC was the lowest at 0.754 (Figure 2c), showing an obvious downward trend. It is

well known that the D-band reflects the structural defects and disorder of carbon, while the G-band is related to graphitic carbon [41,42]. Therefore, a higher R-value indicates more lattice defects of the C atom and a higher graphitization degree on the contrary. Herein, the SC has the lowest graphitization, and the NSC has the highest graphitization, which is consistent with the XRD results.

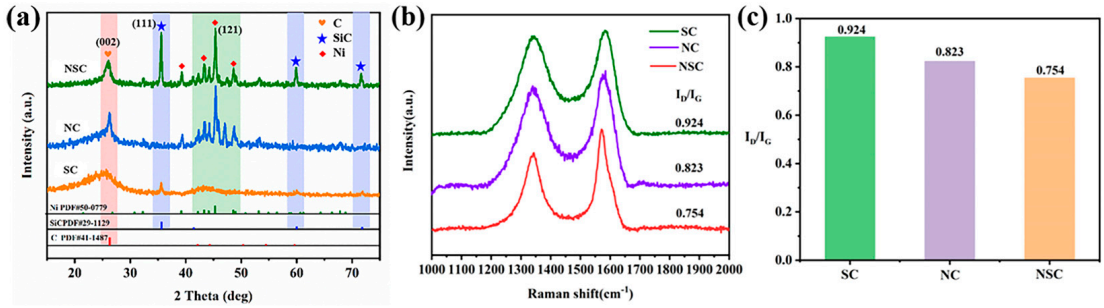

Figure 2. (**a**) XRD patterns; (**b**) Raman spectra; and (**c**) ID/IG graph of all the samples.

The chemical compositions and surface states of the NSC were analyzed by XPS. The XPS full-survey scan spectrum of NSC shown in Figure 3a confirms C, O, Si, and Ni elements. The low strength of the Ni element may be because most of the Ni particles on the surface are coated with C. Figure 3b reveals the high-resolution C 1s spectra, which are deconvoluted into three stripping peaks, where 283.5, 284.6, 285.8 eV can be indexed to the C-Si, C-C, C-O peaks, respectively [43,44]. The Si 2p peak can be fitted into three peaks with typical binding energy of 101.4 and 103.4 eV, which are aligned with the Si-C bond and the Si-O bond [45,46], respectively. Furthermore, the peak with a binding energy of 864 eV is attributed to Ni 2P, and the peaks at 853.1 eV and 873.2 eV are assigned to Ni 2p3/2 and Ni 2p1/2 [47], respectively. Furthermore, the survey spectra of NC and SC are shown in Figure S2. The XPS results are consistent with the XRD results, which proved that the three catalyst materials were successfully synthesized.

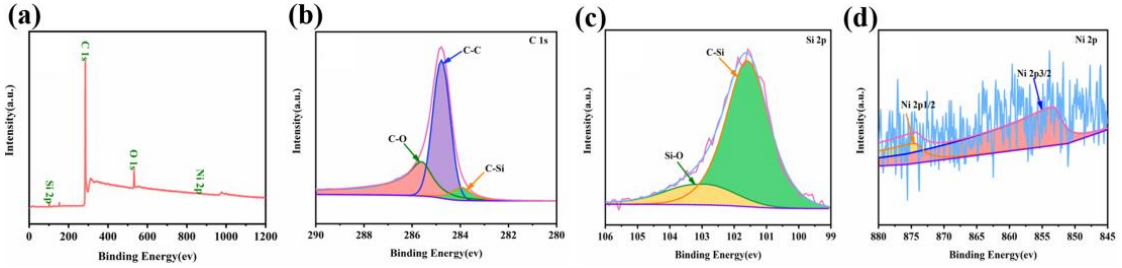

Figure 3. (**a**) XPS full spectrum; (**b**) XPS high-resolution spectrum of C 1s; (**c**) Si 2p; and (**d**) Ni 2p for the NSC composite materials.

The microscopic morphology of the NSC catalyst is revealed by the scanning electron microscopy (SEM) image shown in Figure 4a–d. SEM of NC and SC samples are shown in Figures S3 and S4 in the Supplementary Materials. These nanofibers are highly interconnected with random orientations to form 3D continuous networked structures with excellent mechanical stability [48]. As can be seen in Figure 4a, a large number of highly flexible nanowires grow on the surface of the carbon nanofibers, resulting in a one-dimensional hierarchical structure. Such a microscopic level network not only enhances mechanical connection between fibers but also promotes electron transport and multiple reflections of microwaves in the network, which could benefit the dielectric properties of the hybrid fibers [31].

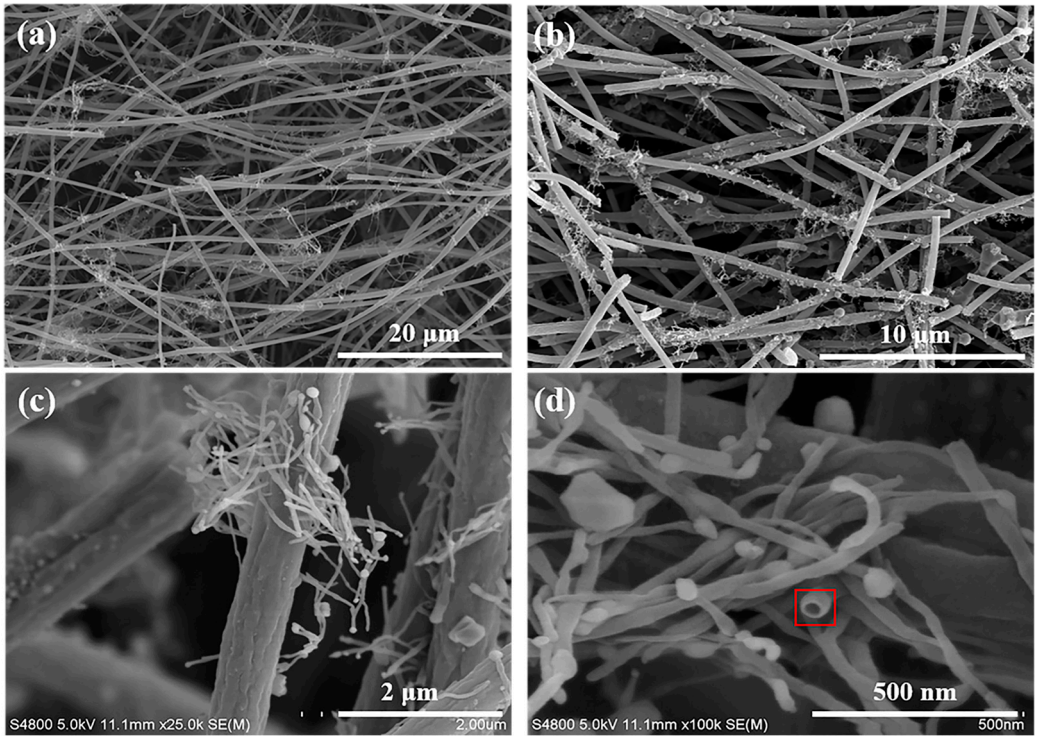

Figure 4. (**a**–**d**) SEM images of NSC catalyst at different magnifications.

TEM and HRTEM analyses were performed to characterize the microstructure in more detail (Figure 5a–h). It is not difficult to see that Ni particles are covered and carbon nanotubes with a diameter of 15 nm grow from the surface of the cover layer, which is caused by Ni nanoparticles catalyzing the graphitization of amorphous carbon at high temperatures [49–51]. Surprisingly, a thin layer of SiC was precipitated on the surface of Ni particles, followed by a graphite carbon layer in the high-resolution HRTEM image in Figure 5d. This occurs because C and Si are solidly dissolved in the molten Ni particles at high temperatures due to the precipitation temperatures of C and SiC being different; C is preferentially precipitated at low temperatures, while SiC is precipitated after nucleation at high temperatures of 1300 °C. Therefore, a SiC, C bilayer structure is formed on the surface of Ni particles. However, due to the lack of silicon sources, SiC can only exist as thin layers [52,53]. Furthermore, such an encapsulated structure can not only effectively protect the metal particles against corrosion in a harsh environment, but also can increase the interface layer between materials, so that the materials can produce more interface polarization under the action of the microwave, and improve the absorption capacity of materials to the microwave [54,55]. HRTEM images show that the periodic lattice fringes with good resolution are about 0.18 nm, 0.25 nm, and 0.35 nm, corresponding to the crystal planes of Ni (002), SiC (111), and C (002), respectively. In Figure 5c, we can see that the surface C layer is bent into a discontinuous sheet; defects will naturally occur at these positions, and a large number of dipoles are easily gathered at the defects, which is conducive to the dipole polarization effect of the absorber, which may lead to electromagnetic wave loss. The high-angle annular dark-field scanning TEM (HAADF-STEM) image and elemental mappings disclose the uniform distribution of C, Ni, and Si throughout the fibrous nanohybrids. It can be seen from Figures S3 and S4 that no nanostructure is generated on the surface of the NC and SC catalysts. Ni nanoparticles of the NC catalyst are uniformly anchored on the surface of the carbon nanofibers, while the SC surface is rough and no nanostructure can be seen from SEM. However, many fine SiC grains were found on the surface and the fibers showed a core–shell structure. There are many interfaces between different catalyst structures. Under the action of a microwave,

the electrons move and gather at the interface, which makes it easy to generate interface polarization and improve the microwave absorption capacity [43].

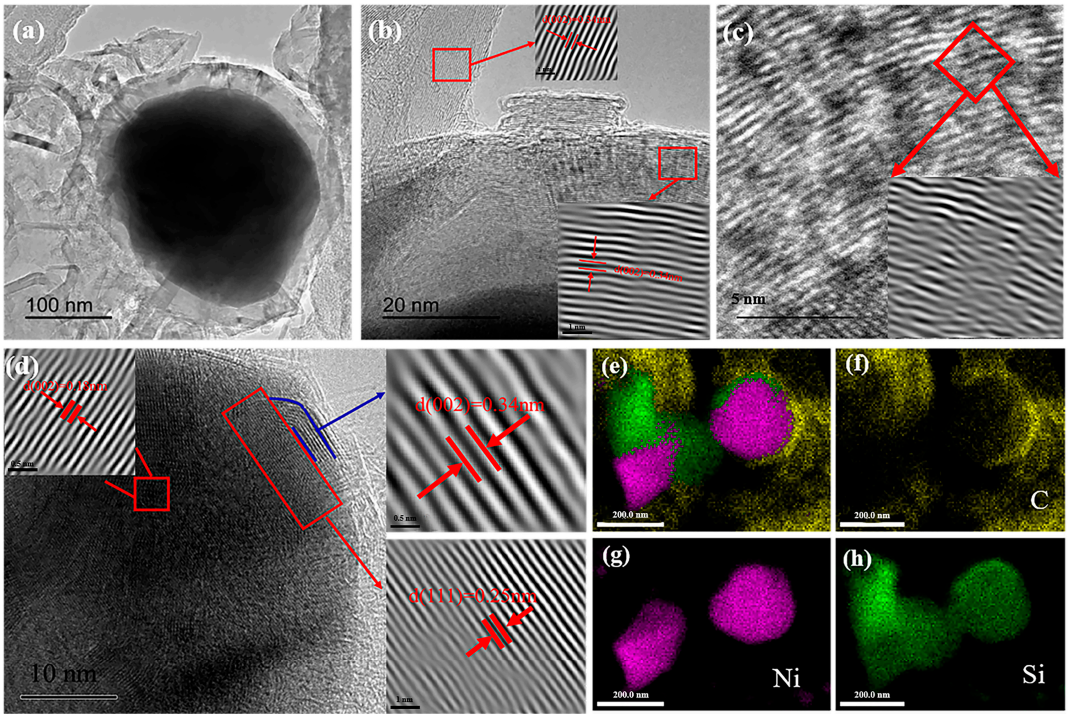

Figure 5. (**a**,**b**) TEM images of NSC catalyst; (**c**,**d**) HRTEM image; (**e**–**h**) EDS Element Mapping Diagram.

3.2. Microwave-Induced Catalytic Degradation of MB

Figure 6 shows the degradation curves of different catalytic materials for the MW catalytic oxidation of methylene blue at a given power in a MW (450 W, 2450 MHz). Before the microwave-assisted degradation of methylene blue, we first soaked these samples with methylene blue solution in the dark for 30 min to achieve adsorption equilibrium. Samples were taken every 30 s until either of the two visually visible samples faded and the test was stopped. The absorption peak of the MB chromophore and the parent ring structure is at 664 nm, so its degradation rate can be determined by the maximum absorption wavelength of 664 nm. By comparing the absorption peaks of the three catalysts at 664 nm, the UV–vis spectra of the NSC, SC, and NC catalysts are shown in Figure S5. It can be found that with the increase in time, the absorption peaks of the NSC catalyst at 664 nm decreased significantly, while the absorption peaks of NC and SC to MB decreased slowly. Figure 6a shows the time-degradation rates of the different catalysts. It can be seen from the figure that the NSC catalyst almost completely degraded after 90 s, with a degradation rate close to 100%, while the degradation rates of SC and NC were about 45% and 19%, respectively. Meanwhile, we tested the degradation performance of the three catalysts without microwave irradiation in order to verify the excitation effect of microwave irradiation on the materials. As can be seen from Figure 6b, the degradation rates of the three catalysts without microwave irradiation were basically around 3%. The results showed that the three catalysts could be excited under microwave irradiation to have certain degradation ability, among which the NSC catalyst could achieve efficient degradation of methylene blue under microwave irradiation. The degradation kinetics results of MB in 90 s is shown in Figure 6c, which indicates that the degradation kinetics of MB in 90 s by the three catalysts under microwave conditions belong to first-order reaction kinetics. The microwave-induced degradation rate constants of MB by different catalysts are shown in Figure 6d. The reaction rates k of NSC, SC, and NC are 0.1951, 0.0100, and 0.0051, respectively. In other words, the degradation rate of MB by NSC is about 19.51 times that of SC and 38.25 times that of NC. By comparing the SC and NC

samples, the degradation efficiency of the SC system is found to be higher than that of NC. It is also confirmed that the presence of SiC in the ternary NSC catalyst contributes more to the degradation than Ni. The above experimental results show that NSC has better MW catalytic activity and higher MB degradation catalytic activity compared with the other two catalysts. In addition, we performed free radical scavenging tests and cyclic degradation tests on the NSC catalysts. As can be seen in Figure 6e, tert-butanol and sodium oxalate were added to the reaction solution as ·OH scavenger, O_2^- scavenger, and h^+ scavenger, respectively, to compare with the degradation of methylene blue by the NSC samples. The addition of tert-butanol and sodium oxalate reduced the degradation rate to 57.8% and 70.4%, respectively, and the degradation of methylene blue was inhibited, which indicated that ·OH, h^+, and O_2^- are important substances leading to the degradation of methylene blue. Through Figure 6f, we found that the NSC catalyst can maintain its original degradation ability after 10 cycles of testing, which indicates that the prepared new catalyst has better stability under microwave action.

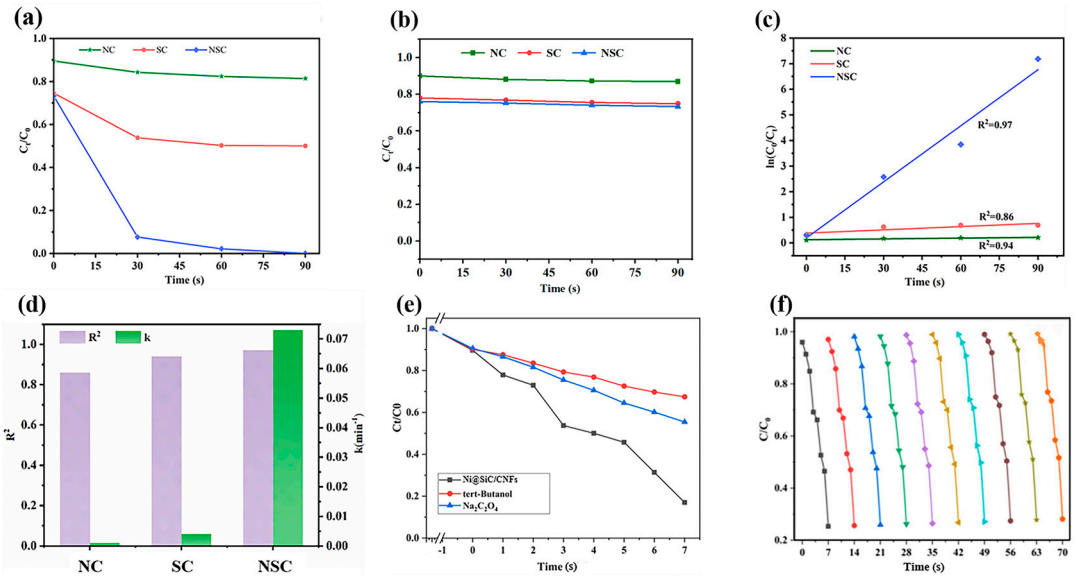

Figure 6. (**a**) Degradation curves of MB by different catalysts under microwave irradiation; (**b**) degradation curves of MB by different catalysts (without microwave irradiation); (**c**) the corresponding degradation rate curve; (**d**) the corresponding degradation slope and R^2 of composites under microwave catalysis; (**e**) free radical scavenging test; (**f**) the cyclic degradation performance of the NSC catalysts.

3.3. Electromagnetic Wave Absorption Characteristics and Catalytic Degradation Mechanism of NSC Composite Materials

To explore the reason why the NSC catalyst has a good degradation efficiency for MB under the action of microwave, we tested the electromagnetic wave absorption performance of the catalyst. Figure 7a–f plotted the electromagnetic parameters of the NSC catalyst to study its electromagnetic wave absorption performance. It is generally true that the −10 dB is equivalent to 90% of the total absorbed energy of the EM wave, and the −20 dB is equivalent to 99% of the total energy absorbed by the EM wave [56]. Reflection loss (RL) data about NSC for a frequency range of 2–18 GHz are illustrated by the curves in Figure 7a. The prepared NSC catalyst exhibits excellent microwave absorption performance, with a maximum reflection loss (RL_{max}) of 51.40 dB at 12.5 GHz. The corresponding matching thickness is 1.418 mm, and the effective RL bandwidth (RL > −10 dB) is 11.4–14.1 GHz.

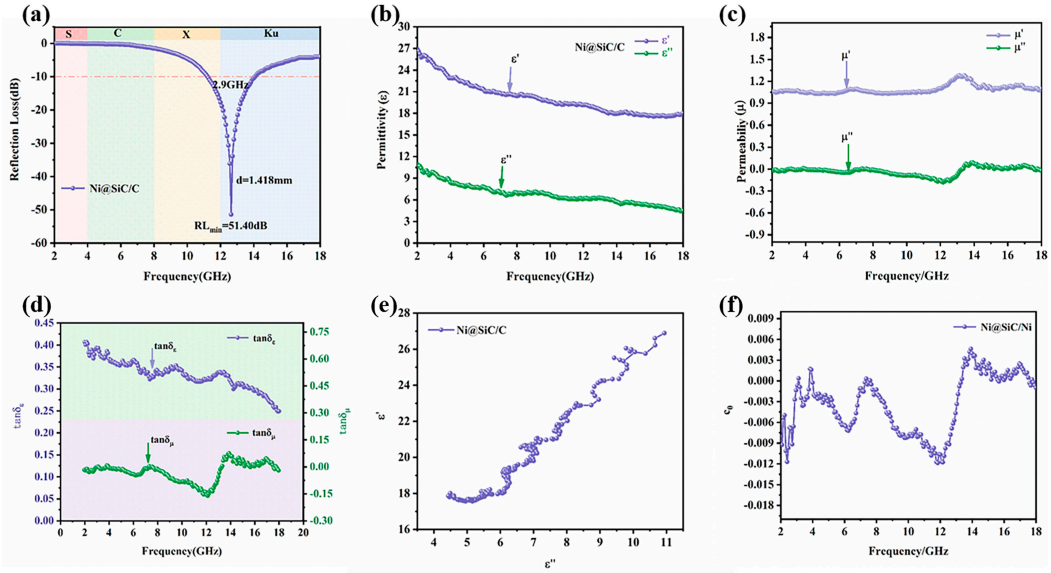

Figure 7. (**a**) RL curves at a thickness of 1.418 mm; (**b**) real/imaginary permittivity of NSC; (**c**) real/imaginary permeability of NSC; (**d**) frequency dependence of dielectric loss and magnetic loss of sample; (**e**) typical Cole–Cole semicircles (ε'' versus ε') for NSC; (**f**) c_0 values of NSC.

As shown in Figure 7b, the permittivity (ε', ε'') of the catalyst decreases gradually with the increase in frequency, which may be related to the polarization and interface relaxation at the interface between the Ni, SiC, and C layer. According to the value of $\tan\delta_\varepsilon$ ($\tan\delta_\varepsilon = \varepsilon''/\varepsilon'$), the dielectric loss capacity is further estimated. Interestingly, the $\tan\delta_\varepsilon$ values of the NSC catalysts peak at 9 GHz and 12.7 GHz, as shown in Figure 7d. The reason is that the dielectric loss ability is affected simultaneously by the polarization effect and by the conductive loss [57].

In addition to dielectric loss, magnetic loss also plays an important role. As shown in Figure 7d, the $\tan\delta_\mu$ value of the catalyst shows a similar trend to the imaginary part (μ'') of the permeability, indicating that the magnetic energy dissipation capacity is the key factor of the magnetic loss [58–60]. It is worth noting that in Figure 7d, the peak of the magnetic loss ($\tan\delta_\mu$) around 13.8 GHz comes from both natural and exchange resonance. It is clearly observed from Figure 7d that the value of $\tan\delta_\varepsilon$ is significantly larger than $\tan\delta_\mu$. This indicates that dielectric loss is the main contributor to excellent microwave absorption performance.

To further investigate the mechanism of dielectric and magnetic loss, Figure 7e–f illustrates the Cole–Cole plots and c_0 curves of the samples. Figure 7e shows the Cole–Cole semicircles of the sample, with each semicircle corresponding to Debye relaxation [61]. Obviously, there are multiple decomposable semicircles in the ε' and ε'' curves, indicating that the Debye relaxation process caused by interfacial polarization and dipole polarization occurs in the samples. In addition, there are almost no straight lines at the ends of the Cole–Cole diagram, indicating that there is almost no conduction loss during the whole process.

The magnetic loss mechanism mainly consists of three parts: exchange resonance, natural resonance, and eddy current loss. In general, the eddy current losses of absorbing materials can be described by the value of c_0 ($c_0 = \mu''(\mu')^{-2}f^{-1}$). When the value of c_0 is constant with increasing frequency, eddy current loss is dominant in magnetic loss. If c_0 changes with f, eddy current losses are suppressed, and natural resonance and exchange resonance are the main sources of magnetic losses [62]. As shown in Figure 7f, the c_0 curve of the sample fluctuates significantly at the frequency of 2–18 GHz, indicating that exchange resonance and natural resonance play a crucial role in the magnetic loss of the catalyst.

Based on the above analysis, the mechanism of degradation of methylene blue by the NSC catalyst under microwave irradiation was further studied, as shown in Figure 8,

and the efficient degradation rate of MB by the binuclear NSC catalyst composed of C, Ni, and SiC is mainly attributed to the following points. (1) The presence of many one-dimensional CNTs in the prepared catalysts is conducive to increasing the electron transport paths during microwave action and increasing the multiple reflections of MW, which gives the materials excellent microwave absorption properties and ensures that the MB can fully absorb microwave energy and convert it into thermal energy during the microwave degradation process. (2) SiC as a polar molecule, under microwave irradiation, will produce dipole polarization. In addition, there are a small number of defects in the catalyst, where the electron aggregation experiences dipole polarization. (3) There are abundant phase boundaries in the composites, which can cause more interfacial polarization and multiple relaxation. The polarization mechanism occurring in processes (2) and (3) will cause the material to generate a lot of heat, putting electrons in an active and unstable state, and the transition will generate hole–electron pairs. At the same time, one-dimensional carbon nanotubes can provide more conductive paths to facilitate the transport of excited hopping electrons. These hole–electron pairs react with O_2 and H_2O in water to form various active substances such as ·OH, O_2^-, and h^+ active substances. (4) Due to the characteristics of microwave selective heating, the dielectric constants of C and SiC in the composite material are different, and there is an obvious difference in the absorption ability of the microwave, which leads to the temperature around the strong wave-absorbing material being significantly higher than that of the weakly absorbing material, and there is a temperature gradient to form a hot spot, and the hot spot generates a high temperature conducive to the generation of the active substances (·OH, O_2^-, and h^+). (5) A unique discharge phenomenon will be produced when the metal is irradiated by microwave. The discharge process will be accompanied by the release of plasma, which not only can shape local high temperatures to strengthen microwave heating, but also can generate plasma which can significantly promote a chemical reaction, which can generate ·OH, O_2^-, and h^+ active substances. Under the action of a microwave, it is the synergistic effect between various elements that makes the degradation of MB (methylene blue) easier to occur.

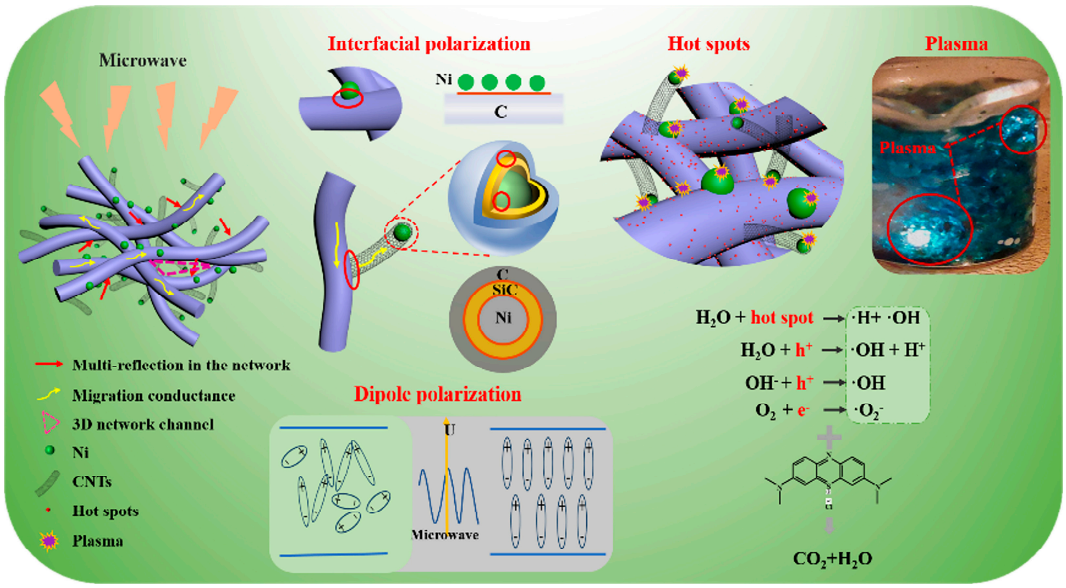

Figure 8. Degradation mechanism of methylene blue by Ni@SiC/CNFs under microwave irradiation.

Overall, the one-dimensional CNT structure extends the conductive path of electrons to enhance microwave dissipation; the polar SiC molecules are more likely to generate dipole polarization under microwave irradiation to enhance the consumption of electromagnetic waves; and the introduction of magnetic Ni particles enriches the depletion mechanism of the material system and generates plasma discharges to generate reactive groups to

promote the reaction under microwave irradiation. The synergistic effect among the three components contributed to the excellent and efficient degradation capability of this catalyst.

4. Conclusions

In this study, catalysts with different structures were successfully prepared by adjusting the raw materials in a precursor solution by the electrostatic spinning method and were then used for the degradation of a high-concentration MB solution under microwave irradiation. The characterization results of the different catalysts suggest that the microstructure of the materials plays an important role in the degradation rate of MB. Under the action of a microwave, the NSC catalyst showed excellent catalytic activity, with MB degradation in 1.5 min. Compared with NC and SC, the reaction rates were 38.25 and 19.51 times higher, which was mainly attributed to the synergistic effect of the thermal effect, non-thermal effect, and plasma effect of the NSC catalyst under the action of the microwave. Under these effects, a large number of ·OH, h^+, and O_2^- active substances were produced, and these active substances could rapidly oxidize methylene blue dye, so that it was rapidly degraded into non-toxic and harmless small molecules. It is expected that Ni@SiC/CNFs with high microwave-assisted catalytic activity will greatly promote a practical application for the removal of organic pollutants.

Supplementary Materials: The following supporting information can be downloaded at: https://www.mdpi.com/article/10.3390/c10030072/s1, Figure S1: Diagram of microwave-assisted catalytic reactor; Figure S2: XPS of the NC and SC composite materials: (a) full spectrum, (b) C 1s, and (c) Ni 2p for the NC composite materials, respectively; (d) full spectrum, (e) C 1s, and (f) Si 2p for the SC composite materials, respectively; Figure S3: (a,b) SEM images of NC catalyst at different magnifications; (c) TEM images of NC catalyst; (d) HRTEM image; Figure S4: (a,b) SEM images of SC catalyst at different magnifications; (c) TEM images of NSC catalyst; (f) HRTEM image; (d–g) HAADF-STEM image and corresponding elemental mappings of (f) C, (g) SiC; Figure S5: Ultraviolet absorption spectra of MB by different composites: (a) C/Ni, (b) C/SiC, (c) Ni@SiC/CNFs.

Author Contributions: Conceptualization, H.O. and J.L.; validation, J.L and L.B.; formal analysis, T.S. and Y.L.; writing—original draft preparation, J.L.; writing—review and editing, C.L. All authors have read and agreed to the published version of the manuscript.

Funding: This research was supported by the National Nature Science Foundation of China (Grant No. 52173299, 52372087).

Data Availability Statement: All original data from the study have been fully included in the article/Supplementary Material and further enquiries can be directed to the corresponding author.

Acknowledgments: The authors would like to thank Jinfan Liu for his help in experimental section.

Conflicts of Interest: The authors declare no conflicts of interest.

References

1. Nasir, A.M.; Awang, N.; Jaafar, J.; Ismail, A.F.; Othman, M.H.D.A.; Rahman, M.; Aziz, F.; Mat Yajid, M.A. Recent progress on fabrication and application of electrospun nanofibrous photocatalytic membranes for wastewater treatment: A review. *J. Water Process Eng.* **2021**, *40*, 101878. [CrossRef]
2. Xia, H.; Li, C.; Yang, G.; Shi, Z.; Jin, C.; He, W.; Xu, J.; Li, G. A review of microwave-assisted advanced oxidation processes for wastewater treatment. *Chemosphere* **2022**, *287*, 131981. [CrossRef]
3. Liu, Z.; Zhang, W.; Liang, Q.; Huang, J.; Shao, B.; Liu, Y.; Liu, Y.; He, Q.; Wu, T.; Gong, J.; et al. Microwave-assisted high-efficiency degradation of methyl orange by using $CuFe_2O_4$/CNT catalysts and insight into degradation mechanism. *Environ. Sci. Pollut. Res. Int.* **2021**, *28*, 42683–42693. [CrossRef] [PubMed]
4. Khoshnam, M.; Farahbakhsh, J.; Zargar, M.; Mohammad, A.W.; Benamor, A.; Ang, W.L.; Mahmoudi, E. α-Fe_2O_3/graphene oxide powder and thin film nanocomposites as peculiar photocatalysts for dye removal from wastewater. *Sci. Rep.* **2021**, *11*, 20378. [CrossRef]
5. Zhang, Y.; Su, P.; Weathersby, D.; Zhang, Q.; Zheng, J.; Fan, R.; Zhang, J.; Dai, Q. Synthesis of γ-Fe_2O_3-ZnO-biochar nanocomposites for Rhodamine B removal. *Appl. Surf. Sci.* **2020**, *501*, 144217. [CrossRef]
6. Wong, S.; Ghafar, N.A.; Ngadi, N.; Razmi, F.A.; Inuwa, I.M.; Mat, R.; Amin, N.A.S. Effective removal of anionic textile dyes using adsorbent synthesized from coffee waste. *Sci. Rep.* **2020**, *10*, 2928. [CrossRef]

7. Liu, Y.; Song, L.; Du, L.; Gao, P.; Liang, N.; Wu, S.; Minami, T.; Zang, L.; Yu, C.; Xu, X. Preparation of Polyaniline/Emulsion Microsphere Composite for Efficient Adsorption of Organic Dyes. *Polymers* **2020**, *12*, 167. [CrossRef] [PubMed]
8. Chen, B.; Long, F.; Chen, S.; Cao, Y.; Pan, X. Magnetic chitosan biopolymer as a versatile adsorbent for simultaneous and synergistic removal of different sorts of dyestuffs from simulated wastewater. *Chem. Eng. J.* **2020**, *385*, 123926. [CrossRef]
9. Xue, C.; Mao, Y.; Wang, W.; Song, Z.; Zhao, X.; Sun, J.; Wang, Y. Current status of applying microwave-associated catalysis for the degradation of organics in aqueous phase—A review. *J. Environ. Sci.* **2019**, *81*, 119–135. [CrossRef]
10. Kubra, K.T.; Salman, M.S.; Hasan, M.N. Enhanced toxic dye removal from wastewater using biodegradable polymeric natural adsorbent. *J. Mol. Liq.* **2021**, *328*, 115468. [CrossRef]
11. Gągol, M.; Przyjazny, A.; Boczkaj, G. Wastewater treatment by means of advanced oxidation processes based on cavitation—A review. *Chem. Eng. J.* **2018**, *338*, 599–627. [CrossRef]
12. Tian, K.; Hu, L.; Li, L.; Zheng, Q.; Xin, Y.; Zhang, G. Recent advances in persulfate-based advanced oxidation processes for organic wastewater treatment. *Chin. Chem. Lett.* **2022**, *33*, 4461–4477. [CrossRef]
13. Liang, C.; Niu, H.-Y.; Guo, H.; Niu, C.-G.; Yang, Y.-Y.; Liu, H.-Y.; Tang, W.-W.; Feng, H.-P. Efficient photocatalytic nitrogen fixation to ammonia over bismuth monoxide quantum dots-modified defective ultrathin graphitic carbon nitride. *Chem. Eng. J.* **2021**, *406*, 126868. [CrossRef]
14. Peng, Y.; Li, Y.; Liu, L.; Hao, X.; Cai, K.; Xiong, J.; Hong, W.; Tao, J. New optimization approach for amphoteric/magnetic ramie biosorbent in dyestuff adsorption. *Biochem. Eng. J.* **2022**, *181*, 108379. [CrossRef]
15. Wang, H.; Zhao, Z.; Zhang, X.; Dong, W.; Cao, Z.; He, L.; Wang, X. Rapid decomplexation of Ni-EDTA by microwave-assisted Fenton reaction. *Chem. Eng. J.* **2020**, *381*, 122703. [CrossRef]
16. Garcia-Costa, A.L.; Zazo, J.A.; Casas, J.A. Microwave-assisted catalytic wet peroxide oxidation: Energy optimization. *Sep. Purif. Technol.* **2019**, *215*, 62–69. [CrossRef]
17. Qi, Y.; Mei, Y.; Li, J.; Yao, T.; Yang, Y.; Jia, W.; Tong, X.; Wu, J.; Xin, B. Highly efficient microwave-assisted Fenton degradation of metacycline using pine-needle-like $CuCo_2O_4$ nanocatalyst. *Chem. Eng. J.* **2019**, *373*, 1158–1167. [CrossRef]
18. Hu, L.; Wang, P.; Liu, G.; Zheng, Q.; Zhang, G. Catalytic degradation of p-nitrophenol by magnetically recoverable Fe_3O_4 as a persulfate activator under microwave irradiation. *Chemosphere* **2020**, *240*, 124977. [CrossRef]
19. Garcia-Costa, A.L.; Zazo, J.A.; Rodriguez, J.J.; Casas, J.A. Microwave-assisted catalytic wet peroxide oxidation. Comparison of Fe catalysts supported on activated carbon and γ-alumina. *Appl. Catal. B Environ.* **2017**, *218*, 637–642. [CrossRef]
20. Lei, Y.; Lin, X.; Liao, H. New insights on microwave induced rapid degradation of methyl orange based on the joint reaction with acceleration effect between electron hopping and Fe^{2+}-H_2O_2 reaction of $NiFeMnO_4$ nanocomposites. *Sep. Purif. Technol.* **2018**, *192*, 220–229. [CrossRef]
21. Shen, M.; Fu, L.; Tang, J.; Liu, M.; Song, Y.; Tian, F.; Zhao, Z.; Zhang, Z.; Dionysiou, D.D. Microwave hydrothermal-assisted preparation of novel spinel-$NiFe_2O_4$/natural mineral composites as microwave catalysts for degradation of aquatic organic pollutants. *J. Hazard. Mater.* **2018**, *350*, 1–9. [CrossRef]
22. Qian, C.; Dai, J.; Tian, Y.; Duan, Y.; Li, Y. Efficient degradation of Fipronil in water by microwave-induced argon plasma: Mechanism and degradation pathways. *Sci. Total Environ.* **2020**, *725*, 138487. [CrossRef] [PubMed]
23. Zhao, C.; Xue, L.; Zhou, Y.; Zhang, Y.; Huang, K. A microwave atmospheric plasma strategy for fast and efficient degradation of aqueous p-nitrophenol. *J. Hazard. Mater.* **2021**, *409*, 124473. [CrossRef] [PubMed]
24. Xu, G.; Jiang, H.; Stapelberg, M.; Zhou, J.; Liu, M.; Li, Q.J.; Cao, Y.; Gao, R.; Cai, M.; Qiao, J.; et al. Self-Perpetuating Carbon Foam Microwave Plasma Conversion of Hydrocarbon Wastes into Useful Fuels and Chemicals. *Environ. Sci. Technol.* **2021**, *55*, 6239–6247. [CrossRef] [PubMed]
25. Zhang, P.; Liang, C.; Wu, M.; Chen, X.; Liu, D.; Ma, J. High-efficient microwave plasma discharging initiated conversion of waste plastics into hydrogen and carbon nanotubes. *Energy Convers. Manag.* **2022**, *268*, 116017. [CrossRef]
26. Pang, Y.; Lei, H. Degradation of p-nitrophenol through microwave-assisted heterogeneous activation of peroxymonosulfate by manganese ferrite. *Chem. Eng. J.* **2016**, *287*, 585–592. [CrossRef]
27. Zhou, J.; You, Z.; Xu, W.; Su, Z.; Qiu, Y.; Gao, L.; Yin, C.; Lan, L. Microwave irradiation directly excites semiconductor catalyst to produce electric current or electron-holes pairs. *Sci. Rep.* **2019**, *9*, 5470. [CrossRef]
28. Pawar, S.P.; Gandi, M.; Bose, S. High performance electromagnetic wave absorbers derived from PC/SAN blends containing multiwall carbon nanotubes and Fe_3O_4 decorated onto graphene oxide sheets. *RSC Adv.* **2016**, *6*, 37633–37645. [CrossRef]
29. Menéndez, J.A.; Arenillas, A.; Fidalgo, B.; Fernández, Y.; Zubizarreta, L.; Calvo, E.G.; Bermúdez, J.M. Microwave heating processes involving carbon materials. *Fuel Process. Technol.* **2010**, *91*, 1–8. [CrossRef]
30. Li, C.; Xia, H.; Zhang, L.; Wang, S.; Peng, J.; Cheng, S.; Shu, J.; Jiang, X.; Zhang, Q. Analysis of dielectric characterization and microwave adsorbing properties in organism-contained spent carbon: An efficient regeneration method via microwave-assisted ultrasound. *Chem. Eng. Process. Process Intensif.* **2018**, *125*, 74–86. [CrossRef]
31. Yuan, X.; Wang, R.; Huang, W.; Kong, L.; Guo, S.; Cheng, L. Morphology Design of Co-electrospinning MnO-VN/C Nanofibers for Enhancing the Microwave Absorption Performances. *ACS Appl. Mater. Interfaces* **2020**, *12*, 13208–13216. [CrossRef]
32. Chen, C.; Xi, J.; Zhou, E.; Peng, L.; Chen, Z.; Gao, C. Porous Graphene Microflowers for High-Performance Microwave Absorption. *Nano-Micro Lett.* **2018**, *10*, 26. [CrossRef]
33. Li, J.; Zhang, F.; Lu, H.; Guo, W.; He, X.; Yuan, Y. Heterogeneous rod-like Ni@C composites toward strong and stable microwave absorption performance. *Carbon* **2021**, *181*, 358–369. [CrossRef]

34. Wang, B.; Wu, Q.; Fu, Y.; Liu, T. A review on carbon/magnetic metal composites for microwave absorption. *J. Mater. Sci. Technol.* **2021**, *86*, 91–109. [CrossRef]
35. Hidaka, H.; Saitou, A.; Honjou, H.; Hosoda, K.; Moriya, M.; Serpone, N. Microwave-assisted dechlorination of polychlorobenzenes by hypophosphite anions in aqueous alkaline media in the presence of Pd-loaded active carbon. *J. Hazard. Mater.* **2007**, *148*, 22–28. [CrossRef]
36. Sun, G.; Dong, B.; Cao, M.; Wei, B.; Hu, C. Hierarchical Dendrite-Like Magnetic Materials of Fe_3O_4, γ-Fe_2O_3, and Fe with High Performance of Microwave Absorption. *Chem. Mater.* **2011**, *23*, 1587–1593. [CrossRef]
37. Ren, Y.; Zhu, C.; Zhang, S.; Li, C.; Chen, Y.; Gao, P.; Yang, P.; Ouyang, Q. Three-dimensional SiO_2@Fe_3O_4 core/shell nanorod array/graphene architecture: Synthesis and electromagnetic absorption properties. *Nanoscale* **2013**, *5*, 12296–12303. [CrossRef]
38. Singh, S.; Bhaskar, R.; Narayanan, K.B.; Kumar, A.; Debnath, K. Development of silicon carbide (SiC)-based composites as microwave-absorbing materials (MAMs): A review. *J. Eur. Ceram. Soc.* **2024**, *44*, 7411–7431. [CrossRef]
39. Singh, S.; Maurya, A.K.; Gupta, R.; Kumar, A.; Singh, D. Improved microwave absorption behavioral response of Ni/SiC and Ni/SiC/graphene composites: A comparative insight. *J. Alloys Compd.* **2020**, *823*, 153780. [CrossRef]
40. Wang, Y.; Di, X.; Chen, J.; She, L.; Pan, H.; Zhao, B.; Che, R. Multi-dimensional C@NiCo-LDHs@Ni aerogel: Structural and componential engineering towards efficient microwave absorption, anti-corrosion and thermal-insulation. *Carbon* **2022**, *191*, 625–635. [CrossRef]
41. Hu, P.; Dong, S.; Li, X.; Chen, J.; Hu, P. Flower-like $NiCo_2S_4$ Microspheres Based on Nanosheet Self-Assembly Anchored on 3D Biomass-Derived Carbon for Efficient Microwave Absorption. *ACS Sustain. Chem. Eng.* **2020**, *8*, 10230–10241. [CrossRef]
42. Liu, L.; Yang, S.; Hu, H.; Zhang, T.; Yuan, Y.; Li, Y.; He, X. Lightweight and Efficient Microwave-Absorbing Materials Based on Loofah-Sponge-Derived Hierarchically Porous Carbons. *ACS Sustain. Chem. Eng.* **2018**, *7*, 1228–1238. [CrossRef]
43. Li, H.; Gao, S.; Tong, H.; Liu, Y.; Wu, A.; Hao, H. The capacitive loss of microwave energy in Ni@SiC@C core/bi-shell nanoparticles. *Chem. Eng. J.* **2022**, *434*, 134655. [CrossRef]
44. Chan, C.K.; Patel, R.N.; O'Connell, M.J.; Korgel, B.A.; Cui, Y. Solution-Grown Silicon Nanowires for Lithium-Ion Battery Anodes. *ACS Nano* **2010**, *4*, 1443–1450. [CrossRef]
45. Liu, Y.; Liu, Y.; Choi, W.C.; Chae, S.; Lee, J.; Kim, B.-S.; Park, M.; Kim, H.Y. Highly flexible, erosion resistant and nitrogen doped hollow SiC fibrous mats for high temperature thermal insulators. *J. Mater. Chem. A* **2017**, *5*, 2664–2672. [CrossRef]
46. Wang, B.; Wang, Y.; Lei, Y.; Wu, N.; Gou, Y.; Han, C.; Fang, D. Hierarchically porous SiC ultrathin fibers mat with enhanced mass transport, amphipathic property and high-temperature erosion resistance. *J. Mater. Chem. A* **2014**, *2*, 20873–20881. [CrossRef]
47. Huo, Y.; Tan, Y.; Zhao, K.; Lu, Z.; Zhong, L.; Tang, Y. Enhanced electromagnetic wave absorption properties of Ni magnetic coating-functionalized SiC/C nanofibers synthesized by electrospinning and magnetron sputtering technology. *Chem. Phys. Lett.* **2021**, *763*, 138230. [CrossRef]
48. Li, T.; Luo, G.; Liu, K.; Li, X.; Sun, D.; Xu, L.; Li, Y.; Tang, Y. Encapsulation of Ni_3Fe Nanoparticles in N-Doped Carbon Nanotube–Grafted Carbon Nanofibers as High-Efficiency Hydrogen Evolution Electrocatalysts. *Adv. Funct. Mater.* **2018**, *28*, 1805828. [CrossRef]
49. Liu, S.; Wang, Z.; Zhou, S.; Yu, F.; Yu, M.; Chiang, C.Y.; Zhou, W.; Zhao, J.; Qiu, J. Metal-Organic-Framework-Derived Hybrid Carbon Nanocages as a Bifunctional Electrocatalyst for Oxygen Reduction and Evolution. *Adv. Mater.* **2017**, *29*, 1700874. [CrossRef] [PubMed]
50. Wu, R.; Wang, D.P.; Rui, X.; Liu, B.; Zhou, K.; Law, A.W.; Yan, Q.; Wei, J.; Chen, Z. In-situ formation of hollow hybrids composed of cobalt sulfides embedded within porous carbon polyhedra/carbon nanotubes for high-performance lithium-ion batteries. *Adv. Mater.* **2015**, *27*, 3038–3044. [CrossRef]
51. Tang, J.; Salunkhe, R.R.; Liu, J.; Torad, N.L.; Imura, M.; Furukawa, S.; Yamauchi, Y. Thermal conversion of core-shell metal-organic frameworks: A new method for selectively functionalized nanoporous hybrid carbon. *J. Am. Chem. Soc.* **2015**, *137*, 1572–1580. [CrossRef] [PubMed]
52. Li, D.; Liao, H.; Kikuchi, H.; Liu, T. Microporous Co@C Nanoparticles Prepared by Dealloying CoAl@C Precursors: Achieving Strong Wideband Microwave Absorption via Controlling Carbon Shell Thickness. *ACS Appl. Mater. Interfaces* **2017**, *9*, 44704–44714. [CrossRef] [PubMed]
53. Huang, F.; Fan, S.; Li, X.; Qu, X.; Tian, Y.; Zhang, X.; Zhang, Z.; Dong, X.; Cao, T. Enhanced dielectric and conductivity properties of carbon-coated SiC nanocomposites in the terahertz frequency range. *Nanotechnology* **2021**, *32*, 265705. [CrossRef] [PubMed]
54. Deng, J.; Ren, P.; Deng, D.; Yu, L.; Yang, F.; Bao, X. Highly active and durable non-precious-metal catalysts encapsulated in carbon nanotubes for hydrogen evolution reaction. *Energy Environ. Sci.* **2014**, *7*, 1919–1923. [CrossRef]
55. Cui, X.; Ren, P.; Deng, D.; Deng, J.; Bao, X. Single layer graphene encapsulating non-precious metals as high-performance electrocatalysts for water oxidation. *Energy Environ. Sci.* **2016**, *9*, 123–129. [CrossRef]
56. Cai, Z.; Su, L.; Wang, H.; Xie, Q.; Gao, H.; Niu, M.; Lu, D. Hierarchically assembled carbon microtube@SiC nanowire/Ni nanoparticle aerogel for highly efficient electromagnetic wave absorption and multifunction. *Carbon* **2022**, *191*, 227–235. [CrossRef]
57. Di, X.; Wang, Y.; Lu, Z.; Cheng, R.; Yang, L.; Wu, X. Heterostructure design of Ni/C/porous carbon nanosheet composite for enhancing the electromagnetic wave absorption. *Carbon* **2021**, *179*, 566–578. [CrossRef]
58. Li, D.; Guo, K.; Wang, F.; Wu, Z.; Zhong, B.; Zuo, S.; Tang, J.; Feng, J.; Zhuo, R.; Yan, D.; et al. Enhanced microwave absorption properties in C band of Ni/C porous nanofibers prepared by electrospinning. *J. Alloys Compd.* **2019**, *800*, 294–304. [CrossRef]

59. Ye, X.; Zhang, J.; Chen, Z.; Xiang, J.; Jiang, Y.; Xie, F.; Ma, X. Microwave absorption properties of Ni/C@SiC composites prepared by precursor impregnation and pyrolysis processes. *Def. Technol.* **2023**, *21*, 94–102. [CrossRef]
60. Wu, F.; Liu, Z.; Wang, J.; Shah, T.; Liu, P.; Zhang, Q.; Zhang, B. Template-free self-assembly of MXene and CoNi-bimetal MOF into intertwined one-dimensional heterostructure and its microwave absorbing properties. *Chem. Eng. J.* **2021**, *422*, 130591. [CrossRef]
61. Huang, B.; Wang, Z.; Hu, H.; Xiu, Z.; Huang, X.; Yue, J.; Wang, Y. Enhancement of the microwave absorption properties of PyC-SiCf/SiC composites by electrophoretic deposition of SiC nanowires on SiC fibers. *Ceram. Int.* **2020**, *46*, 9303–9310. [CrossRef]
62. Li, W.; Guo, F.; Wei, X.; Du, Y.; Chen, Y. Preparation of Ni/C porous fibers derived from jute fibers for high-performance microwave absorption. *RSC Adv.* **2020**, *10*, 36644–36653. [CrossRef] [PubMed]